

Generation Mechanism of Surface and Buried Faults Considering the Effect of Plasticity in a Shallow Crust Structure

K. Wada

Railway Technical Research Institute, Japan

H. Goto

Kyoto University, Japan



SUMMARY:

The ground motion generated by buried rupture earthquakes is empirically larger than that by surface rupture earthquakes in the period range of 0.3-3 seconds. Dynamic rupture propagation is numerically simulated to discuss the generation mechanism by considering the material plasticity in a shallow crust structure. In the case of a deep hypocenter, the stopping front generated from the bottom edge catches up to the rupture front before the rupture passes through the free surface. On the other hands, in the case of a shallow hypocenter, the stopping front does not catch up to the rupture front, and the fault ruptures the surface. The slip rate for the buried faults has a larger peak and a shorter rise time than that for the surface faults in the region close to interface of the shallow crust. The ground motion generated by the source models is consistent with the motion of real earthquakes.

Keywords: Ground motion, Fault rupture, Surface rupture earthquake, Buried rupture earthquake

1. INTRODUCTION

A physical concept for establishing earthquake response spectra is important in discussions on the appropriate input ground motion in seismic designs. In particular, the wave components in a period range of 1-2 s are effective enough to cause damage to buildings and structures. Somerville (2003) reported that the levels of the period range are empirically different between surface and buried rupture earthquakes. The ground motion generated from buried faults is almost always larger than that generated from the surface rupture faults in the period range of 0.3-3 s. The difference in ground motion has been introduced into modern attenuation models by the NGA project (e.g., Abrahamson *et al.*, 2008). Abrahamson *et al.* (2008) compares the depth-to-top-of-rupture scaling of ground motions, and suggests that NGA models incorporating rupture depth dependence for reverse earthquakes with buried ruptures lead to larger PGA than surface ruptures at the same distance.

The locations of the asperities of these earthquakes are also different. Asperities for surface rupture earthquakes are located in regions shallower than 5 km; examples of such earthquakes are San Fernando earthquake (Heaton, 1982), Tabas earthquake (Hartzell and Mendoza, 1991), and Chi-Chi earthquake (Sekiguchi and Iwata, 2001). In contrast, asperities for buried rupture earthquakes are located in regions deeper than about 5 km, Loma Prieta earthquake (Wald *et al.*, 1991), Northridge earthquake (Wald *et al.*, 1996) and Noto Hanto earthquake (Asano and Iwata, 2011) being examples of this type of earthquakes. Note that it is not suggested here that every buried rupture earthquake will have a deep hypocenter. However, this tendency can be discerned in past earthquakes. Although the locations of asperities are different for surface and buried faults, they are similar in terms of their relative positions from the hypocenter. The location of the hypocenter is close to and beneath the asperities. This characteristic follows the indication by Mai *et al.* (2005) that the hypocenter of most earthquakes is located within a region of asperities or very close to one.

Several studies have reported results corresponding to those in Somerville (2003). Kagawa *et al.* (2004) studies asperities from the slip distributions of 20 past earthquakes using the method in Somerville *et al.* (1999), by considering only a rectangular portion of the large slip region, and

discussed the differences in asperity locations between surface and buried faults. They also constructed characterized source models for each fault type and derived results similar to those of Somerville (2003). Dalguer et al. (2008) calibrated the distribution and average value of the stress drop and independently developed dynamic rupture models that agree with observations for surface and buried faults. Their surface fault model incorporates a negative stress drop in the background area where rupture energy is absorbed. On the other hand, their buried fault model has a deeper hypocenter, corresponding to empirical results (Mai *et al.*, 2005). This generates a forward directivity pulse toward the surface. As a result, the rupture of the buried fault generates the high-frequency components of ground motion. This corresponds to empirical results showing that buried faults have larger response spectra in the period range of 0.3-3 s. Pitarka *et al.* (2009) modelled the shallow zone within a thickness of 5 km, containing areas of negative stress drop and lower rigidity, and concluded that the differences in ground motion arise from a combination of the relative weakness of the shallow layer of faults, the relatively larger stress drops of the buried ruptures, and the strong upward directivity from the buried ruptures.

However, most of the results depend on the empirical model parameters, and they cannot explain the fundamental reasons why the fault models become different, e.g. a negative stress drop is observed within a depth of 5 km. In order to clarify the reasons for this, it is necessary to conduct a mechanism-based discussion.

In the present paper, we focus on the inelastic behavior of a shallow crust structure. The effect on the rupture process, off-fault plasticity, has been attributed to the concentration of stress around the rupture front. Poliakov *et al.* (2002) examined stress fields around a rupturing fault embedded in elastic material in order to find the regions where stress levels exceed Mohr-Coulomb failure criterion, and roughly discussed the spatial patterns of off-fault damage. They found that the patterns depend on the major direction of the initial principal stress associated with the fault direction, σ_1 , the direction of rupture propagation, and the rupture velocity. Yamashita (2000) modelled the effect of inelasticity by a reduction in the elastic modulus due to the formation of tensile cracks, and Ando and Yamashita (2007) modelled the effect of inelasticity by generation of branch faults. Andrews (2005) applied a nondilatant Mohr-Coulomb type of yield criterion. He showed that plastic deformation accumulates along the extensional side of a fault and that the width of the plastic zone normal to the fault plane is proportional to the propagation distance. Templeton and Rice (2008) confirmed that the plastic zones depend on the angle between fault direction and the maximum principal stress Ψ and that the simulated results correspond to those of Poliakov *et al.* (2002).

Herein, we apply off-fault plasticity to a shallow crust structure in order to simulate dynamic rupture propagation. Then, we discuss what controls the mechanism of fault extension reaching either the free surface or the buried faults and the generation of different characteristics of the earthquake response spectra.

2. NUMERICAL METHOD

We numerically simulate dynamic rupture propagation on a reverse fault in an elastoplastic 2D space. The simulation method requires accurate calculations and wide versatility in order to introduce elastoplastic materials and a discontinuity over the fault surface. We apply the extended finite element method (X-FEM), which is an advanced type of finite element method (FEM). The detailed methodology and procedures are described in Wada and Goto (2012).

3. SIMULATION MODEL

We consider a reverse fault embedded in a two-layer structure, as shown in Figure 1. Dip angle θ is 45° . The top of the fault is located at the surface, and the bottom is located at a depth of 14.5 km; the width of the nucleation zone is 3 km, and the hypocenter depth is z km. These are the parameters in each analytical case. Layer 1 is 0-5 km in depth, which models the shallow crust structure, and Layer 2 is deeper than 5 km in depth. In Layer 1, density is 2400 g/m^3 ; P wave velocity 4800 m/s; and S wave velocity 2800 m/s. In Layer 2, density is 2670 g/m^3 ; P wave velocity 6000 m/s; and S wave velocity

3460 m/s. The material properties of Layer 2 refer to the materials of the SCEC code validation projects TPV4 (Harris *et al.*, 2009). Internal damping of 2% is considered in Layer 1, while no internal damping is considered in Layer 2, in order to reflect the differences in the damping properties of crust structures.

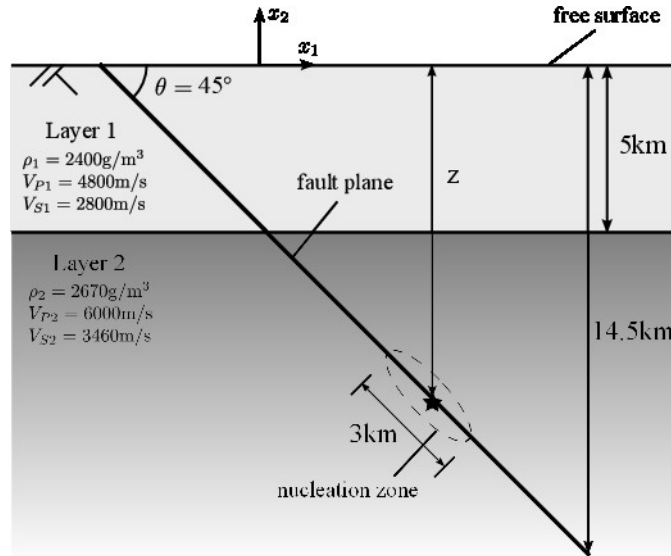


Figure 1. Numerical model and fault geometry. Reverse fault embedded in 2D two-layered model.

The initial stress field is assumed to be a tectonic compressive stress field corresponding to a reverse fault system. Horizontal initial compressive stress is the maximum principal stress, while vertical stress is the minimum principal stress. The coefficient of earth pressure K_0 is set to be 2, which represents the horizontally compressional stress field. The ratio of initial shear traction to initial normal traction μ_0 is represented using K_0 and θ , and μ_0 becomes 1/3 under this condition. The friction parameters for the slip weakening friction law, μ_s , μ_d , D_c , and μ_0 , are shown in Figure 2. Note that the friction parameters are represented by the angles defined by $\phi = \tan^{-1} \mu$. In the nucleation zone, μ_s is set to be $0.95\mu_0$ in order to initiate rupture propagation. The friction parameters are similar to the parameters of the SCEC code validation projects TPV13 (Harris *et al.*, 2009), whereas we modify the parameters in order to generate stable rupture propagation under a compressional stress field. Internal friction angle is also a parameter in each analytical case. The off-fault material becomes constant strength after yielding, which means that it is a perfectly elastoplastic material. Cohesion is 5 MPa at a depth of 0-0.5 km to avoid tensile rupture, and it is 0.2 MPa at a depth of 0.5-14.5 km.

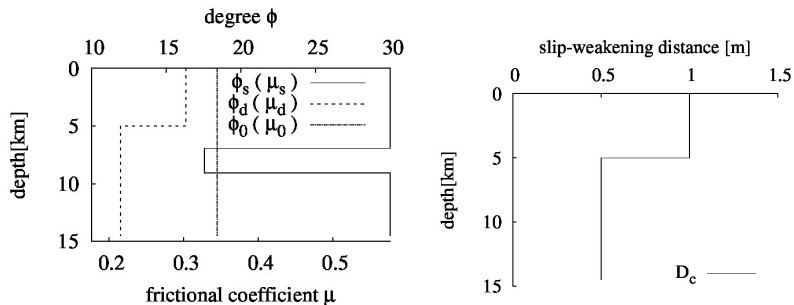


Figure 2. Depth distributions of friction parameters of slip-weakening friction law and ratio of initial shear traction and initial normal traction (left), and slip-weakening distance (right).

4. SIMULATION RESULTS

4.1. Effect of stress drop distribution

We consider two types of depth distributions for the stress drop. One is the depth dependence model (model $\Delta\sigma_{\text{depend}}$, abbreviated as $\Delta\sigma_d$), shown in the left panel of Figure 12, and the other is the constant model (model $\Delta\sigma_{\text{const}}$, abbreviated as $\Delta\sigma_c$), as shown in the right panel of Figure 3. In both models, initial vertical stress is set to be equal to the overburden stress in Layer 1. The stress in Layer 2 of model $\Delta\sigma_d$ is also set to be equal to the overburden stress, while in model $\Delta\sigma_c$, the stress is assumed to be constant. Temporal changes in normal traction during rupture propagation are not considered in our simulations in order to emphasize the effect of changes in confined stress of elastoplastic materials surrounding the fault plane. We consider the internal friction angle for two types of material, namely material ϕ_{same} (abbreviated as ϕ_s) and material ϕ_{weak} (abbreviated as ϕ_w). Material ϕ_s has an internal friction angle of 30° in Layer 1, which is equal to the static frictional angle. This means that the strength of the fault is the same as material strength. In contrast, material ϕ_w has an internal friction angle of 29° in Layer 1, which is unrealistically smaller than the strength of the fault. This is because we emphasize the effect of plasticity on rupture propagation. Both materials have an angle of 50° in Layer 2, which means that the fault plane is clearly weaker. The case name corresponds to the notation (Internal friction angle type)-(Stress drop model).

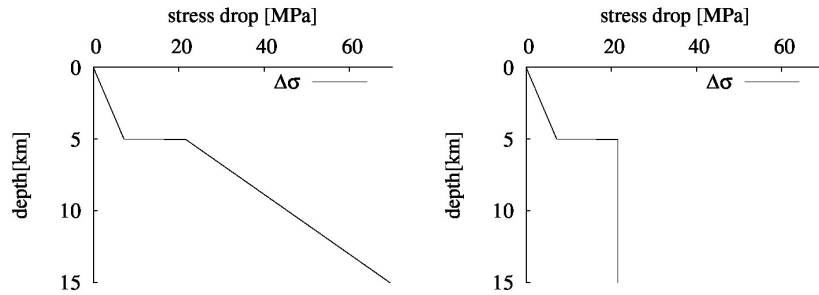


Figure 3. Depth distributions of stress drop: depth-dependant model $\Delta\sigma_d$ (left), and constant model $\Delta\sigma_c$ (right).

Figure 4 shows a comparison of the source rupture process between Case- $\phi_s - \Delta\sigma_d$ and Case- $\phi_w - \Delta\sigma_d$ (Figure 4a), or Case- $\phi_s - \Delta\sigma_c$ and Case- $\phi_w - \Delta\sigma_c$ (Figure 4b). In the time histories of the slip rate for Case- $\phi_s - \Delta\sigma_d$ and Case- $\phi_w - \Delta\sigma_d$, large peak slip rates (40-50 m/s) are obtained in the deep region due to the depth-dependent stress drop. The locations of maximum slip for these cases are deeper than the hypocenter depth of 8 km. On the other hand, the locations are shallower than the hypocenter for Case- $\phi_s - \Delta\sigma_c$ and Case- $\phi_w - \Delta\sigma_c$. Therefore, the cases with constant stress drop model produce more realistic results in terms of the positions of the asperities relative to the hypocenter, as mentioned in the remarks in the introduction. The rupture front propagates in both the upper and lower directions. A stopping front initiates at the bottom end of the fault and propagates in the upper direction. Rupture velocity, the slope of the rupture front, is smaller in Layer 1, compared to cases which do not incorporate the effects of plasticity, namely the elastic case. For Case- $\phi_w - \Delta\sigma_d$ and Case- $\phi_w - \Delta\sigma_c$, the rupture fronts stop in Layer 1 before the stopping front from the bottom edge arrives. When the stopping front arrives, the slip-rate drops to zero. Thus, these fronts result in buried faults.

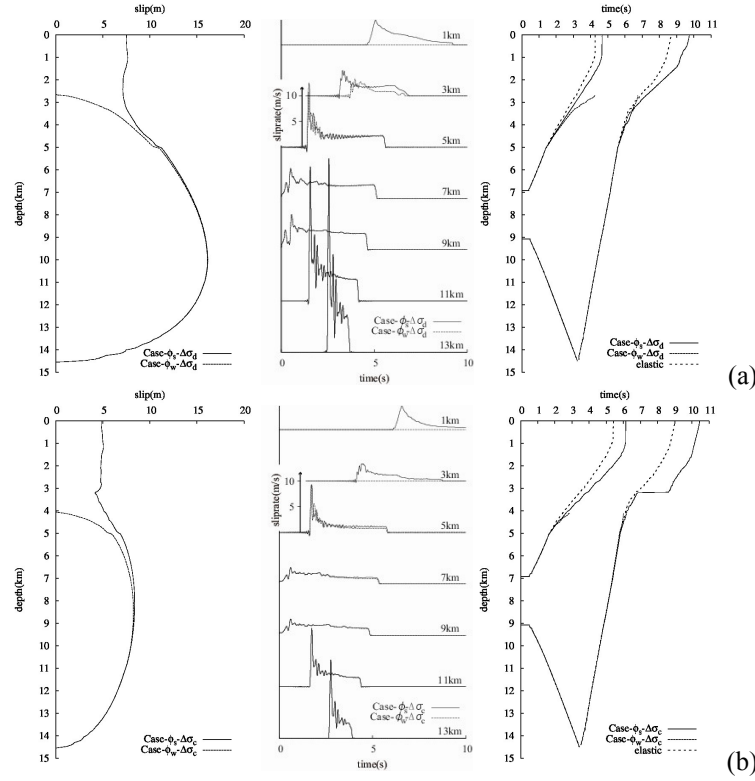


Figure 4. Comparison of depth distribution of slip (left), time history of slip rate (middle) and rupture and stopping fronts (right) between model ϕ_s and model ϕ_w in each stress drop model. (a) stress drop model $\Delta\sigma_d$, and (b) stress drop model $\Delta\sigma_c$.

Figure 5 shows the ratio of response spectra for the model $\Delta\sigma_c$. Observation sites are located 2.5 km and 5 km away from the top of the fault on both hanging and footwall sides, respectively. The ratio of response spectra, namely the spectral ratio is the ratio of acceleration response spectra for Case- ϕ_w - $\Delta\sigma_c$ (buried fault) to that for Case- ϕ_s - $\Delta\sigma_c$ because the rupture for Case- ϕ_s - $\Delta\sigma_c$ becomes a surface fault. When the spectral ratio is larger than 1, the ground motion generated from the buried fault is larger than that generated from the surface fault. The spectral ratio becomes smaller than 1 in almost all of the period range, which indicates that a surface fault earthquake generates larger ground motion than a buried fault earthquake. This is not consistent with the results Somerville (2003).

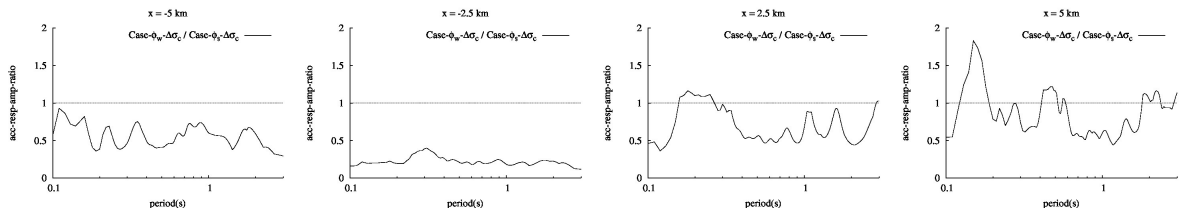


Figure 5. Comparison of ratio of acceleration response spectra of model ϕ_s to the model ϕ_w for stress drop model $\Delta\sigma_c$.

4.2. Effect of hypocenter depth

We compare two cases with different hypocenter depths. One case incorporates a hypocenter depth of 8 km, which is the same as in the cases shown in the previous section. The other has a hypocenter depth of 12 km. The internal friction angles are set to be equal to the model of materials ϕ_s , and the stress drop distribution is equal to the model of $\Delta\sigma_c$. The hypocenter depth denotes the case name.

Figure 6 shows a comparison of the source rupture processes. For Case-z₁₂, the rupture front reaches the bottom of the fault in a few seconds, and the stopping front initiates earlier than in Case-z₈.

Therefore, the stopping front reaches the rupture front, reducing in speed in the shallow crust, and the fault becomes a buried fault. The mechanism of the rupture stopping is represented by the relative position of the hypocenter depth and the bottom depth of the fault, which differs from the mechanism due to the large absorption of energy. Case-z₁₂ generates a smaller slip distribution. This corresponds to smaller magnitude. However, Case-z₁₂ generates a larger peak slip rate (about 15 m/s) at a depth of 6-8 km, because the crack size from the hypocenter is larger, and there is a shorter rise time (about 2 s) due to the early initiation of the stopping front.

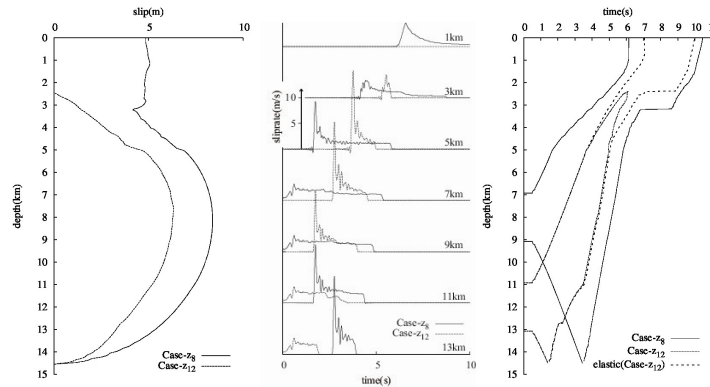


Figure 6. Comparison of depth distribution of slip (left), time history of slip rate (middle), and rupture front and stopping fronts (right) between different hypocenter depths

Figure 7 shows the horizontal ground velocity and the spectral ratio. Arrival times and phases differ between the two cases due to the different hypocenter depths. On the hanging wall side ($x = 2.5$ km, 5 km), the ground velocity for Case-z₁₂ has a larger peak and a shorter duration time. This is because the slip rate for Case-z₁₂ has a larger peak and a shorter rise time at a depth of 6-8 km. On the other hand, on the footwall side ($x = -2.5$ km, -5 km), the ground velocity for Case-z₈ has a larger peak and a longer duration time. This illustrates the effect of the slip rate near the surface (at a depth of 1-2 km), that is, the effect of the stress drop near the surface. Seismic waves generated at a depth of 6-8 km need to travel a longer distance to the footwall side than waves generated at a depth of 1-2 km. Therefore, the spectral ratio on the hanging wall side is larger than 1, which corresponds to real earthquakes (Somerville, 2003), while surface fault earthquakes generate larger response spectra on the footwall side.

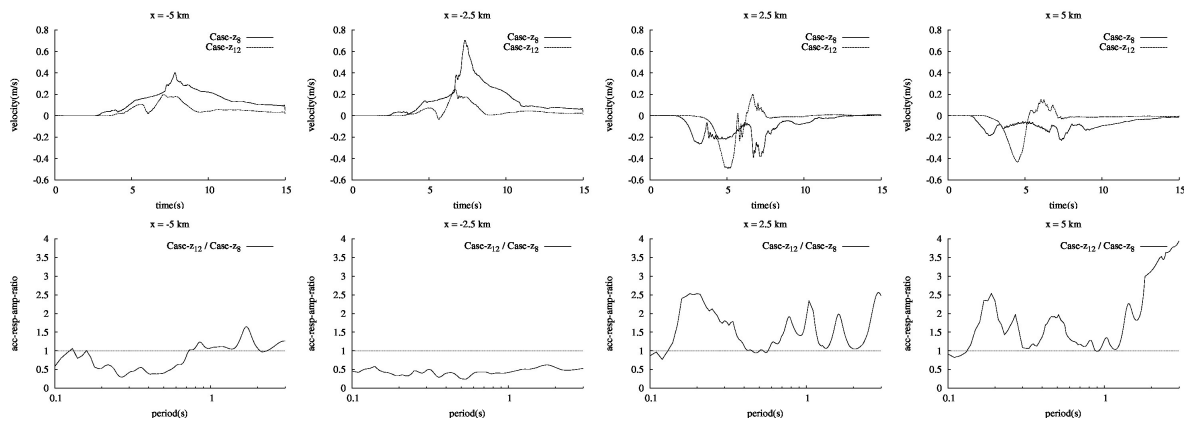


Figure 7. Comparison of time history of horizontal ground velocities (top) and ratio of acceleration response spectra (bottom) of different hypocenter depths.

Somerville (2003) does not explicitly discuss the differences in ground motion between the hanging wall and footwall sides. However, the attenuation curve by Abrahamson and Silva (1997) used as the average spectrum includes the hanging wall effect. Therefore, we consider that the tendency discussed in Somerville (2003) should be satisfied in both hanging wall and footwall sides.

4.3. Reduction in the effect of the stress drop near the surface

In order to reduce the effect of the stress drop near the surface, we set the dynamic frictional coefficient in the shallow crust to increase linearly in relation to the static frictional coefficient from the deeper parts to the surface. This means that a fault close to the surface is not a weak plane, and gradually merges with the perfectly elastoplastic material. Figure 8 shows the depth distribution of frictional coefficients and the corresponding distribution of the stress drops. Figure 8a illustrates the model where μ_d is changed from a depth of 1 km, model $\Delta\sigma_{1\text{km}}$. In this model, the stress drop distribution is parabolic because both μ_d and the fault normal traction change linearly. The stress drop becomes negative near the surface; however, it naturally becomes zero at the surface. Figure 8b illustrates the model where μ_d is changed from a depth of 2 km, model $\Delta\sigma_{2\text{km}}$. Both models have the same stress drop as model $\Delta\sigma_c$ in Layer 2. All cases have the internal frictional angle as model ϕ_s . The case names are indicated by (Stress drop model)-(Hypocenter depth).

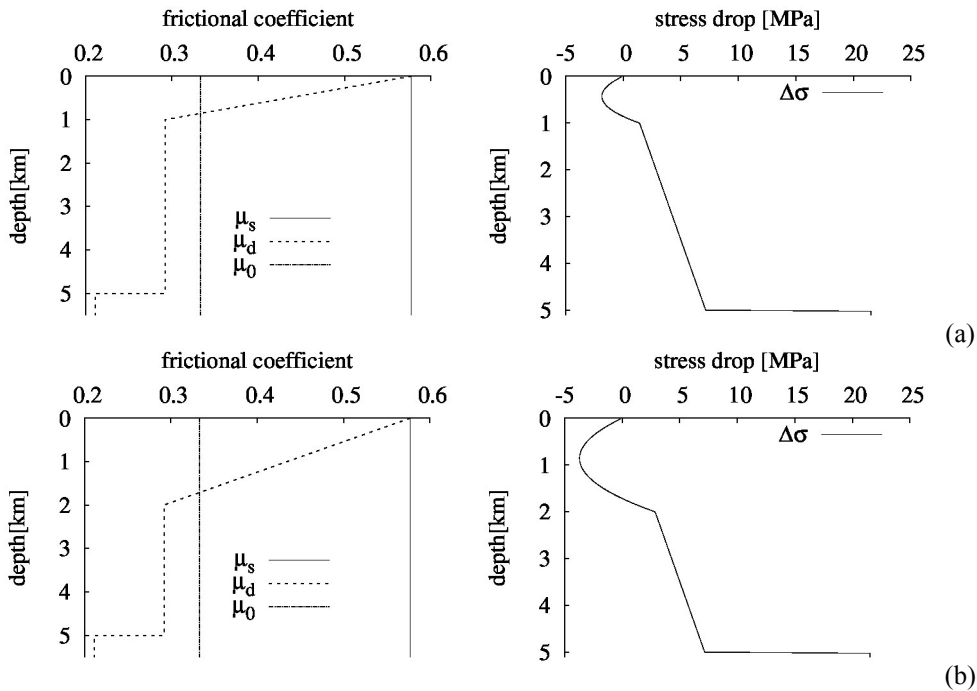


Figure 8. Depth distribution of frictional coefficient and corresponding distribution of stress drop. (a) dynamic frictional coefficient changes from depth of 1 km, model $\Delta\sigma_{1\text{km}}$, and (b) changes from depth of 2 km, model $\Delta\sigma_{2\text{km}}$.

Figure 9 shows compares slip distributions and slip-rate time histories for different stress drop models. The slip rates at down-dip coordinates indicated by the numbers on the right side of the panel are shown. Slips near the surface for Case- $\Delta\sigma_c$ -z₈ are the largest, and magnitude decreases for Case- $\Delta\sigma_{1\text{km}}$ -z₈ and decreases further for Case- $\Delta\sigma_{2\text{km}}$ -z₈. This corresponds to stress drops near the surface. The peak slip rate for Case- $\Delta\sigma_{1\text{km}}$ -z₈ is smaller than that for Case- $\Delta\sigma_c$ -z₈, while the rise time is similar. On the other hand, the peak slip rate and the rise time for Case- $\Delta\sigma_{2\text{km}}$ -z₈ are smaller and shorter than those for the other cases. As shown in Figure 10, peak velocity becomes smaller as the stress drop near the surface is reduced. This effect is significant near the top of the fault but becomes less significant for the sites far from the top. Therefore, ground motion near the fault for surface faults is greatly affected by stress drops near the surface. The spectral ratio of Case- $\Delta\sigma_c$ -z₁₂ to Case- $\Delta\sigma_{2\text{km}}$ -z₈ has the largest value; it is larger than 1 not only on the hanging wall sides ($x = 2.5$ km, 5 km), but also on the footwall sides ($x = -5$ km) in the period range of 1-2 s.

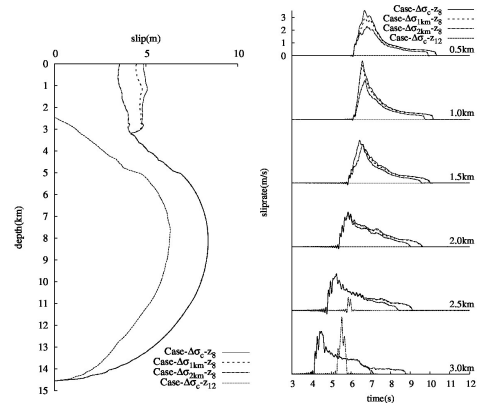


Figure 9. Comparison of depth distribution of slip (left) and time history of slip rate (right) among different stress drop models $\Delta\sigma_c$, $\Delta\sigma_{1km}$ and $\Delta\sigma_{2km}$.

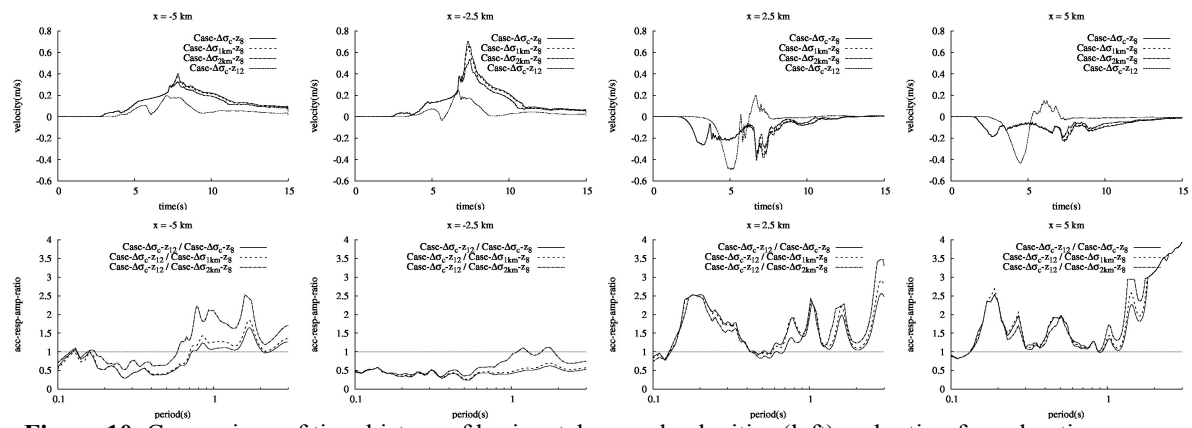


Figure 10. Comparison of time history of horizontal ground velocities (left) and ratio of acceleration response spectra (right) among different stress drop models $\Delta\sigma_c$, $\Delta\sigma_{1km}$ and $\Delta\sigma_{2km}$.

5. COMPARISON WITH CHARACTERIZED SOURCE MODEL

Kagawa *et al.* (2004) constructed characterized source models for each fault type based on kinematic inversion results from actual earthquakes. In the models, the surface fault has asperities with small stress drops in regions shallower than 5 km depth, and both faults have asperities with large stress drops in regions shallower than 5 km depth. Note that the definition of stress drop for the characterized source model, defined by the seismic moment and the area of asperities, is different from that of the dynamic source model. In order to clarify the difference in definition, the stress drop for the characterized source model is called the kinematic stress drop. The kinematic stress drop is evaluated from the space derivative of the final slip distribution. Figure 11 shows the depth distribution of the kinematic stress drop and final slip normalized by the average slip calculated from the results of our dynamic simulations. The kinematic stress drop for the buried fault earthquake is larger in regions deeper than 2.5 km depth. The surface fault has a small kinematic stress drop in regions shallower than 2.5 km depth. In both cases, large kinematic stress drops are calculated in 2.5-5 km depth, and small stress drops are located in regions around 8 km depth where the final slips become maximum. The features are similar to the characterized source models described by Kagawa *et al.* (2004).

While we cannot conclude that the dynamic simulations represent real fault rupture exactly, the comparison results suggest that our simulation results are at least consistent with the existent characterized source models. In other words, physical meanings of the characterized source models are explained by the simulation results provided in this study.

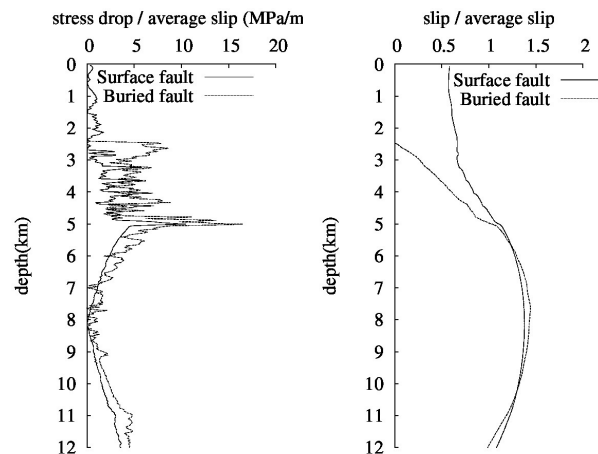


Figure 11. Depth distributions of kinematic stress drop (left) and final slip normalized by average slip (right).

6. CONCLUSIONS

We have discussed the generation mechanism of surface and buried faults by considering the effect of plasticity in a shallow crust structure. The stress drop is considered to be constant in the deep crust zone in order to obtain asperities shallower than the hypocenter depth, corresponding to real earthquakes. The effect of plasticity decreases the rupture velocity in the shallow crust structure with the same friction angles for both static friction of the fault and the materials. As a result, in the case of a deep hypocenter, the stopping front generated from the bottom edge catches up with the rupture front before the rupture passes through the free surface. On the other hand, in the case of a shallow hypocenter, the stopping front does not catch up with the rupture front, and the fault ruptures the surface. The slip rate for the buried fault has a larger peak and a shorter rise time than that for the surface fault at a depth of 6-8 km. Therefore, buried fault earthquakes have a larger response, in the period range of 0.3-3 s, which corresponds to real earthquakes. Finally, our source models are consistent with characterized source models in terms of the depth distribution of the kinematic stress drop.

ACKNOWLEDGEMENT

We are grateful to the following people for providing useful information and for discussions: Professor Sumio Sawada, Professor Yoshikazu Takahashi, and many other researchers who supplied us with important data. This study was supported in part by a Grant-in-Aid for Young Scientists B of the Japan Society for the Promotion of Science.

REFERENCES

- Abrahamson, N. and Silva, W. (1997). Empirical response spectral attenuation relations for shallow crustal earthquakes. *Seism. Res. Lett.*, **68**, 94-127.
- Abrahamson, N., Atkinson, G., Boore, D., Bozorgnia, Y., Campbell, K., Chiou, B., Idriss, I.M., Silva, W., and Youngs, R. (2008). Comparisons of the NGA ground-motion relations. *Earthquake Spectra*, **24**, 45-66.
- Ando, R. and Yamashita, T. (2007). Effects of mesoscopic-scale fault structure on dynamic earthquake ruptures : Dynamic formation of geometrical complexity of earthquake faults. *J. Geophys. Res.*, **112**, B09303.
- Andrews, D. J. (2005). Rupture dynamics with energy loss outside the slip zone. *J. Geophys. Res.*, **110**, B01307.
- Asano, K. and Iwata, T. (2011). Source-Rupture Process of the 2007 Noto Hanto, Japan, Earthquake Estimated by the Joint Inversion of Strong Motion and GPS Data. *Bull. Seism. Soc. Am.*, **101**, 2467-2480.
- Dalguer, L. A., Miyake, H., Day, S. M., and Irikura, K. (2008). Surface Rupturing and Buried Dynamic-Rupture Models Calibrated with Statistical Observations of Past Earthquakes. *Bull. Seism. Soc. Am.*, **98**, 1147-1161.
- Harris, R. A., Barall, M., Archuleta, R., Dunham, E., Aagaard, B., Ampuero, J. P., Bhat, H., Cruz-Atienza, V., Dalguer, L., Dawson, P., Day, S., Duan, B., Ely, G., Kaneko, Y., Kase, Y., Lapusta, N., Liu, Y., Ma, S., Oglesby, D., Olsen, K., Pitarka, A., Song, S., and Templeton, E. (2009). The SCEC/USGS dynamic

- earthquake rupture code validation exercise. *Seism. Res. Lett.*, **80**, 119-126.
- Hartzell, S. and Mendoza, C. (1991). Application of an iterative least-squares waveform inversion of strong-motion and teleseismic records to the 1978 Tabas, Iran, earthquake. *Bull. Seism. Soc. Am.*, **81**, 305-331.
- Heaton, T. (1982). The 1971 San Fernando earthquake: A double event? *Bull. Seism. Soc. Am.*, **72**, 2037-2062.
- Kagawa, T., Irikura, K., and Somerville, P. (2004). Differences in ground motion and fault rupture process between the surface and buried rupture earthquakes. *Earth Planets Space.*, **56**, 3-14.
- Mai, P., Spudich, P., and Boatwright, J. (2005). Hypocenter Locations in Finite-Source Rupture Models. *Bull. Seism. Soc. Am.*, **95**, 965-980.
- Pitarka, A., Dalgner, L. A., Day, S. M., Somerville, P., and Dan, K. (2009). Numerical Study of Ground-Motion Differences between Buried-Rupturing and Surface-Rupturing Earthquakes. *Bull. Seism. Soc. Am.*, **99**, 1521-1537.
- Poliakov, A. N. B., Dmowska, R., and Rice, J. R. (2002). Dynamic shear rupture interactions with fault bends and off-axis secondary faulting. *J. Geophys. Res.*, **107**, 2295.
- Sekiguchi, H. and Iwata, T. (2001). The source process of the 1999 Chi-Chi, Taiwan, earthquake in semi-long period (2-20s). *Annual Report on Active Fault and Paleoseismic Researches*, **1**, 315-324.
- Somerville, P. (2003). Magnitude scaling of the near fault rupture directivity pulse. *Phys. Earth Planet. Int.*, **137**, 201-212.
- Templeton, E. L. and Rice, J. R. (2008). Off-fault plasticity and earthquake rupture dynamics: 1. Dry materials or neglect of fluid pressure changes. *J. Geophys. Res.*, **113**, B09306.
- Wada, K. and Goto, H. (2012). Generation mechanism of surface and buried faults: Effect of plasticity in a shallow crust structure, *Bull. Seism. Soc. Am.*, in printing.
- Wald, D., Heaton, T., and Hudnut, K. (1996). The slip history of the 1994 Northridge, California, earthquake determined from strong-motion, teleseismic, GPS, and leveling data. *Bull. Seism. Soc. Am.*, **86**, S49-S70.
- Wald, D., Helmlinger, D., and Heaton, T. (1991). Rupture model of the 1989 Loma Prieta earthquake from the inversion of strong-motion and broadband teleseismic data. *Bull. Seism. Soc. Am.*, **81**, 1540-1572.
- Yamashita, T. (2000). Generation of microcracks by dynamic shear rupture and its effects on rupture growth and elastic wave radiation. *Geophys. J. Int.*, **143**, 395-406.